Journal Code: C N M | Article ID 2 5 2 5 | Dispatch: 30.10.12 | No. of Pages: 18 | CE: | ME:

INTERNATIONAL JOURNAL FOR NUMERICAL METHODS IN BIOMEDICAL ENGINEERING
Int. J. Numer. Meth. Biomed. Engng. (2012)
Published online in Wiley Online Library (wileyonlinelibrary.com). DOI: 10.1002/cnm.2525

Hemodynamic variations due to spiral blood flow through four patient-specific bifurcated stent graft configurations for the treatment of abdominal aortic aneurysms

Florian Stefanov [1], Tim McGloughlin [2], Patrick Delassus [1] and Liam Morris [1,*,†]

[1] *Galway Medical Technologies Centre (GMedTech), Department of Mechanical and Industrial Engineering, Galway Mayo Institute of Technology, Galway, Ireland*
[2] *Centre for Applied Biomedical Engineering Research and Materials and Surfaces Sciences Institute, Department of Mechanical and Aeronautical Engineering, University of Limerick, Ireland*

UNCORRECTED PROOF

SUMMARY

Endovascular repair is now a recognised procedure for treating abdominal aortic aneurysms. However, post-operative complications such as stent graft migration and thrombus may still occur. To assess these complications numerically, the correct input boundary conditions, which include the full human aorta with associated branching, should be included. Four patient-specific computed tomography scanned bifurcated stent grafts (SGs) were modelled and attached onto a full human aorta, which included the ascending, aortic arch and descending aortas. Two of the SG geometries had a twisted leg configuration, while the other two had conventional nontwisted leg configurations. Computational fluid dynamics was completed for both geometries and the hemodynamics assessed. The complexity of the flow patterns and secondary flows were influenced by the inclusion of the full human aorta at the SG proximal section. During the decelerating phase significant recirculations occurred along the main body of all SG configurations. The inclusion of the full human aorta did not impact the velocity contours within the distal legs and there was no difference in drag forces with the SG containing the full human aorta and those without. A twisted leg configuration further promoted a spiral flow formation along its distal legs. Copyright © 2012 John Wiley & Sons, Ltd.

Received 26 April 2012; Revised 18 September 2012; Accepted 7 October 2012

KEY WORDS: spiral flow; stent graft configurations; abdominal aortic aneurysms; human aorta; drag force; stent graft thrombus

1. INTRODUCTION

Abdominal aortic aneurysm (AAA) is a cardiovascular disease that is characterised by localised expansion of the abdominal aorta wall because of a degenerative arterial disease that induces local arterial wall weakening. About one person in 1000 develops an abdominal aortic aneurysm between the ages of 60 and 65, and this number continues to rise with age. Screening studies show that abdominal aortic aneurysms occur in 2% to 13% of men and 6% of women over the age of 65. A continually growing aneurysm can rupture causing heavy bleeding into the abdominal region, which can lead to death in almost 90% of cases. AAAs are the 13th cause of death in men over 55 years of age in the US [1–7].

Endovascular aneurysm repair (EVAR) is now recognised as an effective alternative to conventional open surgery for treating patients with AAAs since it was first introduced into clinical practice in 1991 [8–11]. In EVAR, a stent graft is deployed into the affected abdominal region by over-the-wire techniques through the femoral artery and thus shielding the weakened AAA

*Correspondence to: Liam Morris, Galway Medical Technologies Centre (GMedTech), Department of Mechanical and Industrial Engineering, Galway Mayo Institute of Technology, Galway, Ireland.

†E-mail: liam.morris@gmit.ie

Copyright © 2012 John Wiley & Sons, Ltd.

wall from the pulsatile blood flow [12–15]. The minimally invasive nature of EVAR results in early-recovery, reduced mortality and morbidity when compared with conventional surgical repair [16, 17]. However, post-operative complications beyond the first year, such as stent graft migration, endoleaks, stent graft thrombus, endotension and device failure may still occur [18–22].

Several computational studies have been done on assessing the drag forces acting on idealised [23] and patient-specific [24–29] bifurcated stent graft models, while others [24] assessed the hemodynamics through conventional and tapered grafts. These computationally derived drag forces can be compared with experimentally obtained migration forces required for displacing stents [30–32].

Computational modelling can be influenced significantly by the geometry and input boundary conditions. There have been numerous studies carried out on curved vessels to establish the influence of vessel curvature, Reynolds number, Dean's number and Womersley number on the flow patterns [33–40]. Papaharilaou *et al*. [41] showed that out-of-plane models create a bulk rotation of the velocity profile that sets up a Dean type flow in contrast to a planar model. Also, Myers *et al*. [42] found Dean-like secondary flow features in the right coronary artery, which were found to be extremely sensitive to the local curvature effects. Large curvature induces a significant enhancement of the secondary flow velocity effect and a greater axial flow reversal along the aortic arch [43]. Various experimental studies have shown pulsating flow, curvature and branches along the human aorta induces Dean like forces, that creates a vortex formation and transient separation below the renal arteries [44–47]. Shearing of blood across the lumen can damage red blood cells [48]. This shearing is further amplified because of the strong curvature effects, out of plane curvature and branching. Recirculations and eddies can contribute to enhanced deposition of blood particulates along the arterial wall. Previous numerical and experimental studies on blood flow characteristics in the human aorta have included the four branching arteries (celiac, superior mesenteric, left and right renal arteries) and the curvature and taper in the abdominal aorta [44–47, 49–51] and with the inclusion of bifurcated stent graft [27, 52, 53]. However, all of these studies have assumed a fully developed flow input before the branching arteries. Shipkowitz *et al*. [54] performed a steady flow simulation on an idealised human aorta (neglecting out of plane curvature), which included both renal arteries and an inlet velocity profile obtained from MRI with an added rotational velocity effect. Their studies revealed the importance of secondary motion in the descending aorta on the flow patterns found in the branches downstream. *In vivo* studies have shown the existence of secondary flows in the descending aorta in the form of a clockwise rotation in systole and a counter clockwise rotation in diastole [35, 55]. MRI velocity contour slices have shown skewness of the blood flow patterns at the supraceliac and infrarenal locations [56]. This rotational effect can be attributed to the complex flow patterns created at the exit of the aortic arch and the curvature of the descending aorta [35, 36, 57].

All the numerical studies regarding patient specific cases, to date, for assessing device performance after EVAR, have involved flat velocity profile inputs at either the supraceliac or infrarenal locations. It is clear from the literature that numerical studies within the human aorta must include the ascending aorta, aortic arch, descending aorta and the associated branches. To date no studies have been conducted on bifurcated stent grafts for the treatment of AAAs, which include the whole human aorta. The main purpose of this study is to assess the effects that input boundary flow conditions can have on the hemodynamics through four patient-specific bifurcated stent graft nontwisted and twisted leg configurations with the inclusion of the full human aorta.

2. METHODS

2.1. Geometry reconstruction

Five patient-specific computed tomography (CT) images were obtained in DICOM (Digital Imaging and Communications in Medicine) format from the Midwestern Regional Hospital, Limerick, St. James Hospital, Dublin and McGowan Institute for Regenerative Medicine, Pittsburgh, USA. All of these patients were suffering from AAAs. The first model was the full human aorta,

UNCORRECTED PROOF

Copyright © 2012 John Wiley & Sons, Ltd.

DOI: 10.1002/cnm

which included the ascending, aortic arch and descending aortas, while the other four models were post-operative scans of bifurcated stent grafts. The CT scan parameters for the medical data were: slice thickness of 2.5 mm, resolution (pixels) of 512 × 512 and pixel size of 0.7159 mm. The DICOM files were thresholded in which a three-dimensional (3D) smoothed volume was generated with Mimics (Materialise, Mimics v14.0, Belgium) enclosed by a triangulated fitted surface. All 3D models were exported as a binary STL (Standard Tessellation Language) format as shown in Figures 1(A) and (B). Eight simulations were ran with four simulations containing the full human aorta and the other four without the human aorta. The flow created from the full human aortic model was applied to all stent graft inlets (two of the four models attached to the full human aorta are shown in Figures 1(A) and (B)), and this ensured the same velocity profiles entering all models. The other four simulations without the human aorta had a flat velocity profile imposed at the inlet, which corresponded to the same flowrate as the stent graft models containing the human aorta distal to renal arteries. Figure 1(C) shows two conventional nontwisted leg and two twisted leg stent graft configurations.

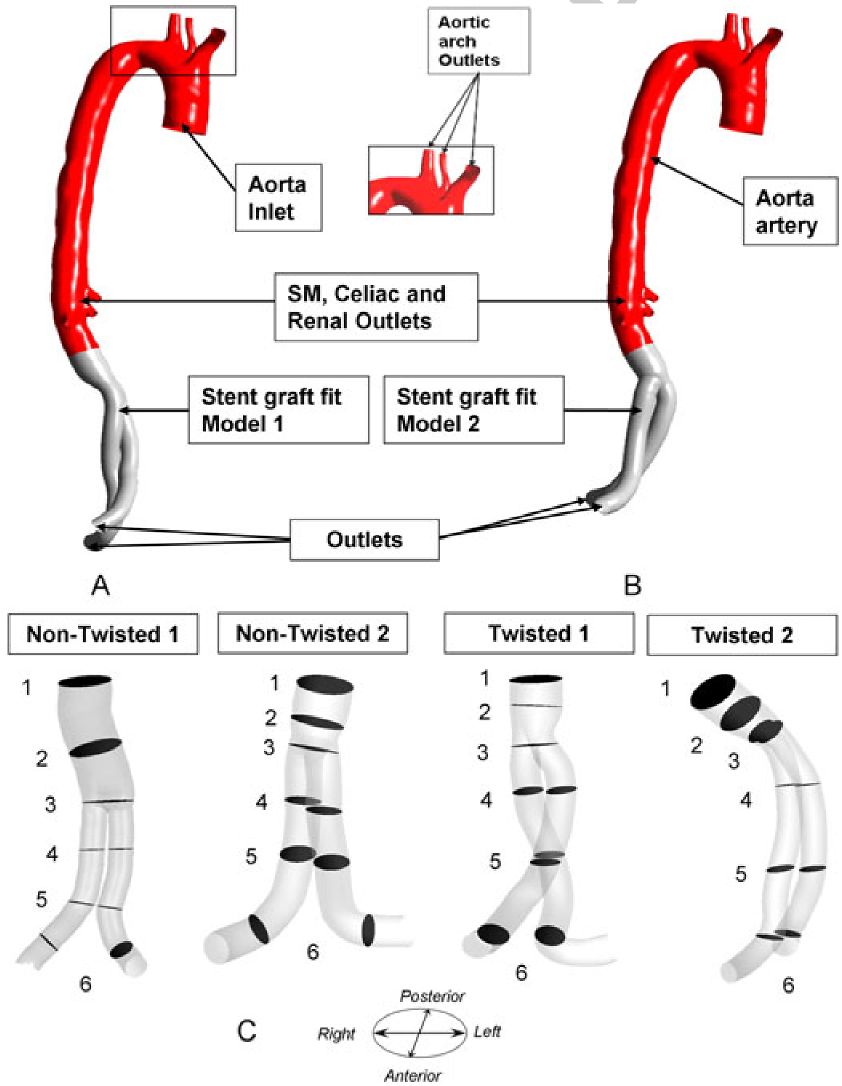

Figure 1. Stent graft fits STL geometries attached to the human aorta. (A) Twisted 1, (B) nontwisted 2 and (C) all stent graft models.

Color Online, B&W in Print

Copyright © 2012 John Wiley & Sons, Ltd.

DOI: 10.1002/cnm

2.2. Meshing

F2 All the models, in binary STL format, were meshed within ICEM (Ansys ICEM, Manufacture 13.0) to generate the fluid domain. A structured hexahedral mesh, applying the O-grid meshing technique, was used to mesh all fluid domains. Between 900,000 to 1,020,000 mesh elements were applied. Figures 2(A) and (B) present the O-grid meshing scheme distribution throughout the computational domains.

2.3. Boundary conditions

T1 Infrarenal blood flow characteristics are extremely complex and are affected by the four major outflow vessels just below the diaphragm; these are the celiac, superior mesenteric and the left/right renal arteries and the blood flow exiting the aortic arch [35, 36, 47, 57]. During resting conditions, these four vessels that branch off the aorta receive approximately two thirds of the total descending thoracic aortic blood flow. Table I shows the percentage of blood flow through the major vessels within the human aorta during resting. For resting conditions on a range of subjects varying in age from 20 to 70 years, it was found by MRI scanning that the resting flowrate can vary between 1 to 3 L/min at the supraceliac and infrarenal locations respectively [56, 59]. For our simulations, flow through the inferior mesenteric artery was neglected.

A commercially available software ANSYS (Ansys CFX solver v.13.0) was used to solve the governing equations of motion, using a coupled algebraic multigrid approach involving finite ~~elements~~ domain discretization. At the inlet of the aortic artery, flow rate boundary condition

UNCORRECTED PROOF

Color Online, B&W in Print

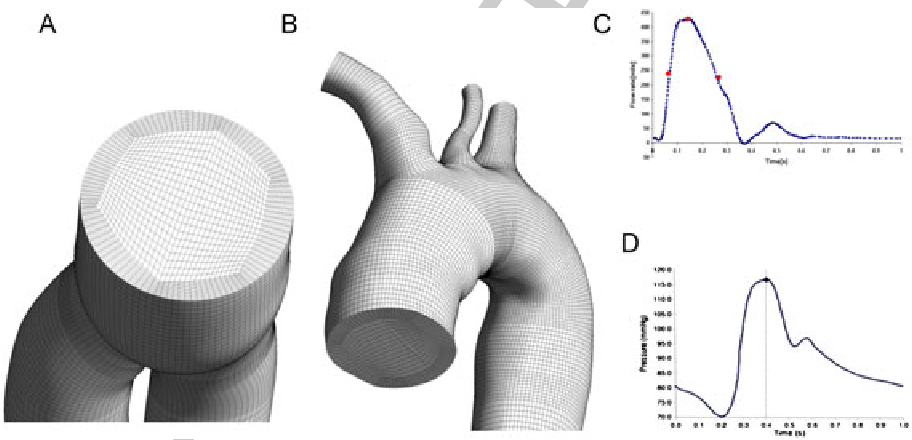

Figure 2. Computational fluid domain of aorta and stent graft fit hexahedral mesh display and boundary conditions. (A) Cross-section of twisted 1 mesh, (B) aortic arch mesh, (C) inlet flow rate and (D) outlet pressure waveforms [58].

Table I. Proportion of blood flow through the major arteries of the aorta [44, 45].

Artery	Rest
Brachiocephalic	5%
Left common carotid	5%
Left subclavian	5%
Celiac	19%
Superior mesenteric (SMA)	12%
Left renal	12%
Right renal	12%
Left iliac	15%
Right iliac	15%

Copyright © 2012 John Wiley & Sons, Ltd.

DOI: 10.1002/cnm

Table II. Carreau–Yasuda parameters to model the non-Newtonian characteristic of blood [61].

μ_0(Pa·s)	μ_∞(Pa·s)	λ (s)	n	a
0.16	0.0035	8.2	0.2128	0.64

was assigned for both models, while at the outlets, a pressure waveform boundary was assigned for both stent graft fit outlets (as shown in Figures 2(C) and (D)), and controlled flow rates by percentages were assigned individually for each of the aortic outlets as shown in Table I [58, 60]. Blood was assumed to be a non-Newtonian fluid with a density of 1050 kg/m^3 and a dynamic viscosity described by the Carreau–Yasuda model in Equation (1).

$$\frac{\mu - \mu_\infty}{\mu_0 - \mu_\infty} = \left[1 + (\lambda\dot{\gamma})^a\right]^{(n-1)/a} \tag{1}$$

where $\dot{\gamma}$ denotes the scalar shear rate. This model was used to account for the shear-thinning behaviour of blood. Table II shows the Carreau–Yasuda parameters (viscosities μ_0 and μ_∞- lower and upper ends of the shear rate range and λ, n, a define the transition between these extreme conditions) to model blood's constitution properties [61].

A transient CFD analysis was performed for five cardiac cycles (cycle time = 1 s) to achieve pulse cycle independence. The fluid time step was set to 0.005 s. Rigid wall and laminar flow boundary condition were assigned to the models.

2.4. Mesh independence

The fluid mesh of the models was declared independent when the peak velocity at the outlet did not change by more than ±2% between successive meshes. Pulse cycle independence was achieved after four cardiac cycles. The convergence criteria for mass and momentum residuals were 1×10^{-4} and 1×10^{-6}, respectively. The CFD analysis was performed on a 64-bit Dell Precision T3500 (CPU: Intel Xeon Quad core 2.67 GHz with 6 GB of RAM). One cardiac cycle took 18 h.

3. RESULTS

3.1. Geometrical effects

The 3D models generated from the CT scans show that each stent graft device adapted its shape after deployment to that of the aorta, generating particular geometric variations in terms of proximal and bifurcation leg angles. Table III presents the geometric characteristics for all stent graft fits. The variation in the Reynold's number, radius of curvature and Dean's number along the distal leg's centreline is shown for the nontwisted leg configuration in Figure 3 and the twisted leg configurations in Figure 4. Dean's number (*De*) is the ratio of the effective centrifugal inertial forces

Table III. Geometric measurements for model 1 and 2.

Type and location of measurement	Nontwisted 1	Nontwisted 2	Twisted 1	Twisted 2
Proximal neck diameter[mm]	25	24	24	24
Distal leg diameter [mm]	15	16	17	15
Proximal length [mm]	56	22	29	28
Distal length [mm]	98	110	127	130
Leg angle at bifurcation [Degrees]	58	62	36	40
Proximal anterior/posterior neck angle [Degrees]	7	9.8	21.3	13
Proximal lateral neck angle [Degrees]	9	14.3	26.5	62
Configuration	Noncrossed legs	Noncrossed legs	Crossed legs	Crossed legs

UNCORRECTED PROOF

Copyright © 2012 John Wiley & Sons, Ltd.

DOI: 10.1002/cnm

Color Online, B&W in Print

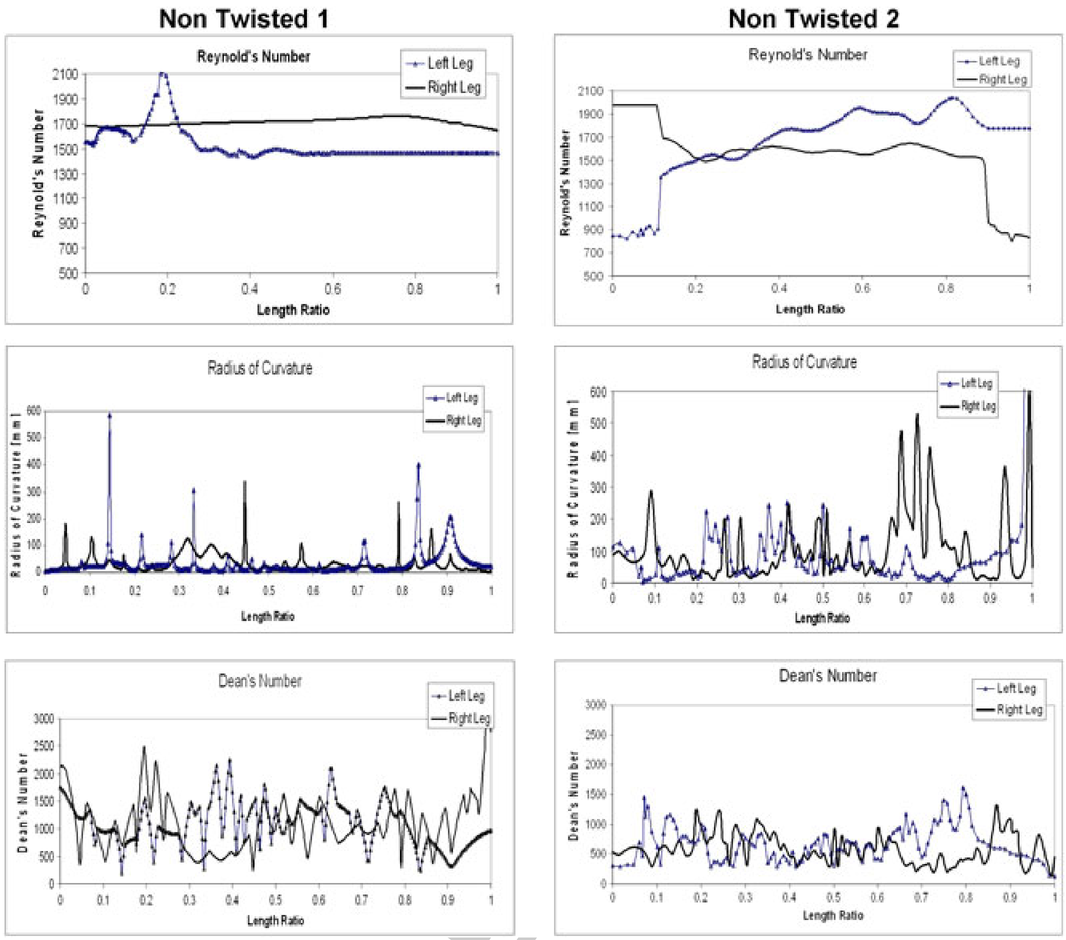

Figure 3. Reynolds number, radius of curvature and Dean's number for both nontwisted configurations.

UNCORRECTED

to the viscous forces. With increasing *De*, the effects of the centrifugal forces become stronger and increase the secondary velocities. Dean's number is an analytical solution to fully developed flow in curved tubes and is given by a nondimensional parameter ~~(Dean, 1927;1928).~~

$$De = Re\sqrt{\left(\frac{r}{R}\right)} \tag{2}$$

where *Re* is the Reynolds number, *R* is the radius of curvature and *r* is the radius of the lumen along the line of the radius of curvature. The diameters along each leg was obtained automatically within the MIMICS software [illegible]utting planes, which were orthogonal to each vessel's centreline. The centreline for each model was further smoothed by the rlowess function available in MATLAB V7.0.1 [illegible]e rlowess function is a lowess smoothing method that is resistant to outliers. Table IV shows the average Reynolds number, radius of curvature and Dean's number for both legs for each stent graft model.

The Mann–Whitney nonparametric confidence interval test was applied in MINITAB 16.2.0 statistical software (State College, PA, USA) to assess if there was any significant geometrical or flow parameter differences between all stent graft models. The radius of curvature and Dean's number were used to quantify the geometrical and flow parameter variations, respectively. At the 95% confidence interval the left leg of nontwisted 2 had a median radius of curvature greater than

Copyright © 2012 John Wiley & Sons, Ltd.

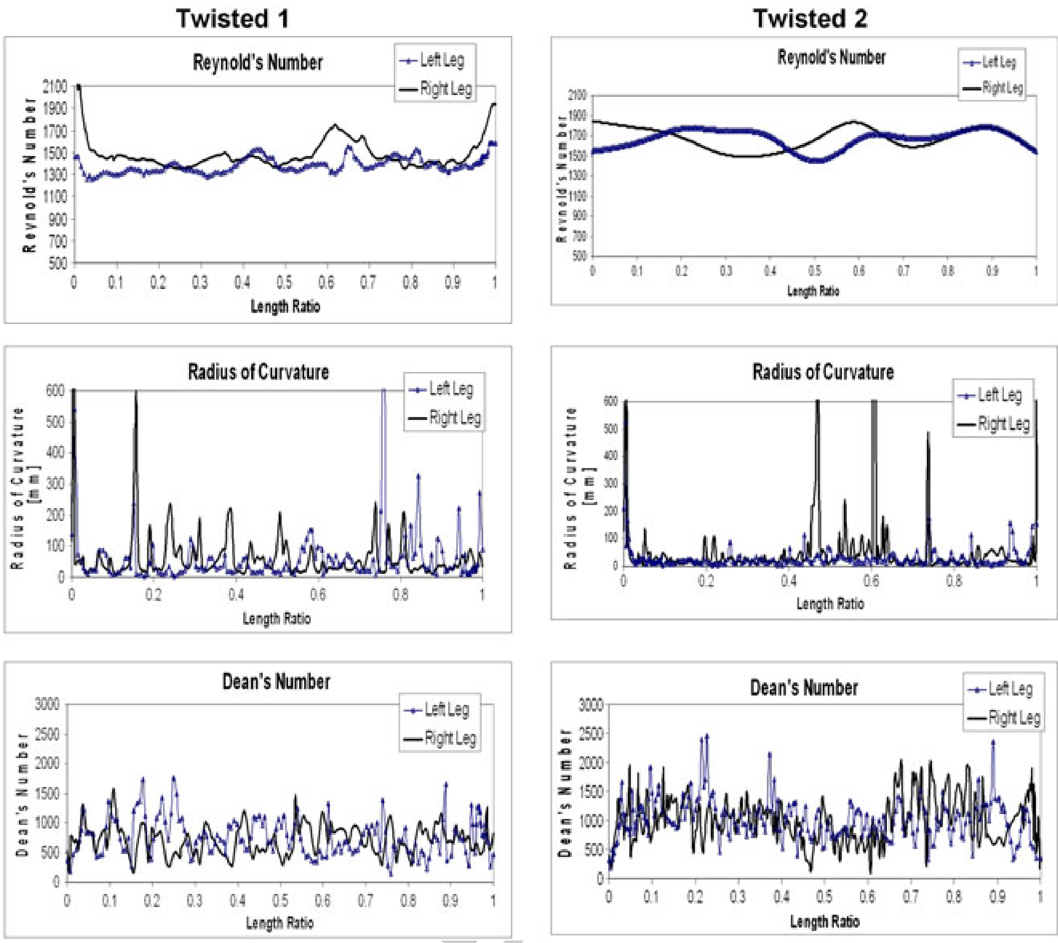

Figure 4. Reynolds number, radius of curvature and Dean's number for both twisted configurations.

Color Online, B&W in Print

UNCORRE

Table IV. Average values for Reynolds number, radius of curvature and Dean's number for both legs of all stent graft models.

	Reynolds number		Radius of curvature [mm]		Dean's number	
Model	Left	Right	Left	Right	Left	Right
Nontwisted 1	1673	1675	33	32	1088	1092
Nontwisted 2	1663	1533	87	100	681	597
Twisted 1	1388	1509	57	65	772	717
Twisted 2	1540	1708	30	60	1016	1023

twisted 1, which in turn was greater than nontwisted 1 and twisted 2. There was no significant difference in the radius of curvature between the left legs of nontwisted 1 and twisted 2. Nontwisted 1 had the highest Dean's number with twisted 2 being higher than twisted 1 and nontwisted 2 having the lowest Dean's number for the left leg. For the right leg there was no significant difference in radius of curvature between the nontwisted 1 and twisted 2 configurations with twisted 1 having a higher radius of curvature and nontwisted 2 having the highest. Also, there was no significant difference in Dean's number for the nontwisted 1 and twisted 2 with these two configurations having the highest Dean's number and nontwisted 2 having the lowest for the right leg.

Copyright © 2012 John Wiley & Sons, Ltd.

DOI: 10.1002/cnm

Color Online, B&W in Print

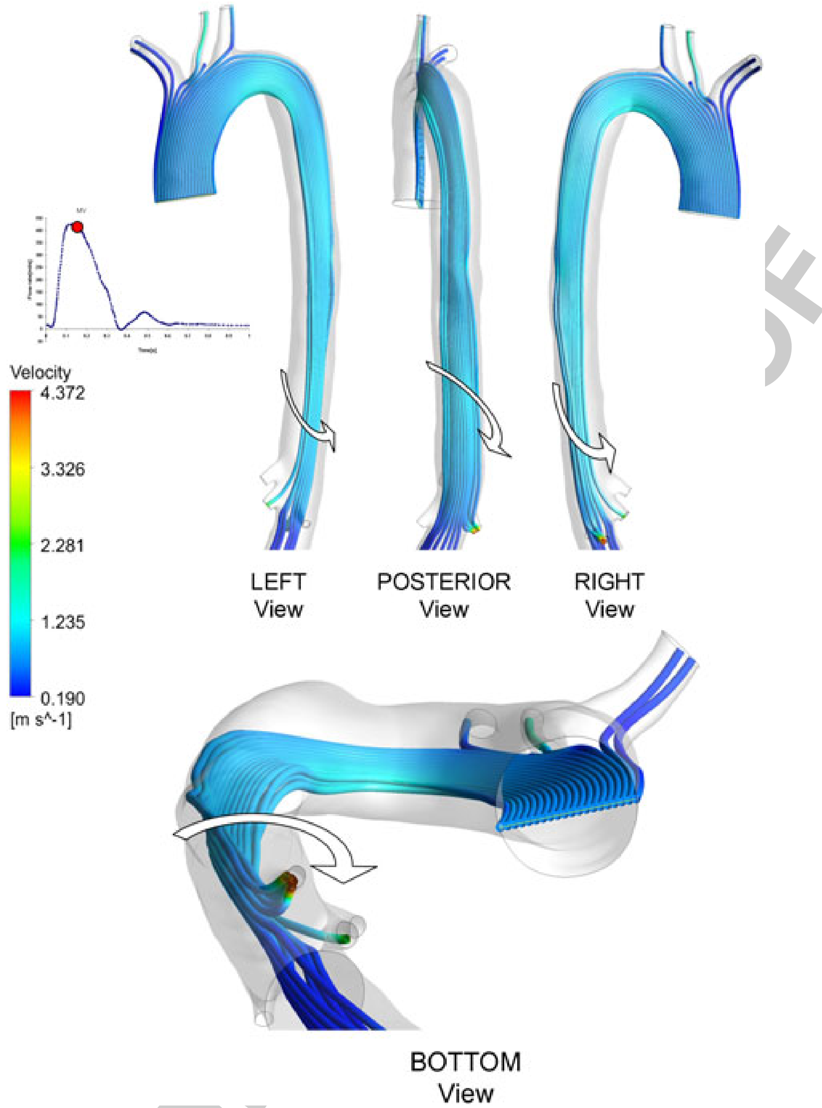

Figure 5. Spiral flow of velocity streamlines through the full human aorta at maximum velocity.

3.2. Stent grafts inlet flow profile — generated from the aortic arch

The flow skewed towards the inner wall of the proximal end of all stent graft configurations in a spiral manner as shown in Figure 5. The influence the full human aorta with the seven branches have on the flow patterns for maximum velocity and maximum deceleration is shown in Figures 6 to 9. These figures show six cross-sectional velocity contour plots corresponding to the sections shown in Figure 1(C) for the four stent graft configurations with and without the full human aorta.

3.3. Drag force magnitude and orientation

The drag force components on X, Y and Z axis and the corresponding resultant forces were computed for the fifth cardiac cycle for all cases as shown in Figures 10(A)–(D) with the drag force direction over one cardiac cycle given in Figure 10(E) and the drag force orientation at maximum pressure given by Figure 10(F). Table V shows the maximum drag force and drag force orientation angles occurring at maximum blood pressure with φ being the maximum change in drag force angle over one cardiac cycle and θ is the maximum force orientation angle with respect to the X-axis.

Copyright © 2012 John Wiley & Sons, Ltd.

DOI: 10.1002/cnm

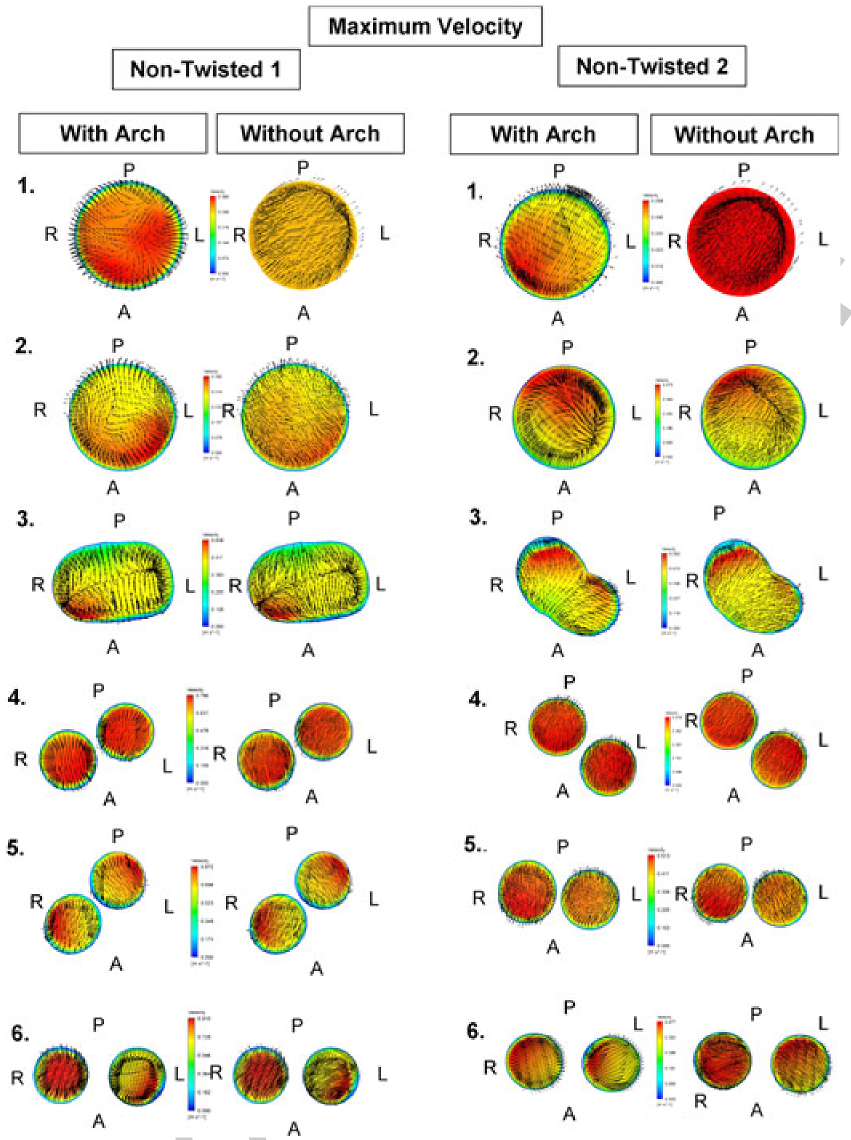

Figure 6. Velocity contour section plots along both nontwisted configurations with and without the full human aorta attached at maximum velocity.

Color Online, B&W in Print

4. DISCUSSION

This skewing of the flow towards the inner wall of the proximal end of all stent graft models was directly related with the general skewing of the blood flow towards the inner wall at the entrance of the aortic arch and midway along the aortic arch, as shown in Figure 5. Also, there was a recirculation region at the inner wall at the exit of the arch with the fluid skewed towards the inner wall. This flow result is in accordance with experimental findings [35, 36, 57, 62–64]. Along the descending aorta the flow starts off being skewed towards the outer wall and rotates from the outer to the inner wall in an anticlockwise rotation. This anticlockwise rotation is due to the secondary flows in the descending aorta. *In vivo* studies have shown the existence of this anticlockwise rotation in the descending aorta during systole [35, 55]. Figures 6–9 show a comparison of the velocity contours at six locations for all stent graft models with and without the full human aorta. For the maximum velocity condition all the inlet velocity profiles were highly skewed. Depending on the proximal ends geometry the flow was either skewed towards the left/anterior (nontwisted 1), right/anterior

Copyright © 2012 John Wiley & Sons, Ltd.

DOI: 10.1002/cnm

Color Online, B&W in Print

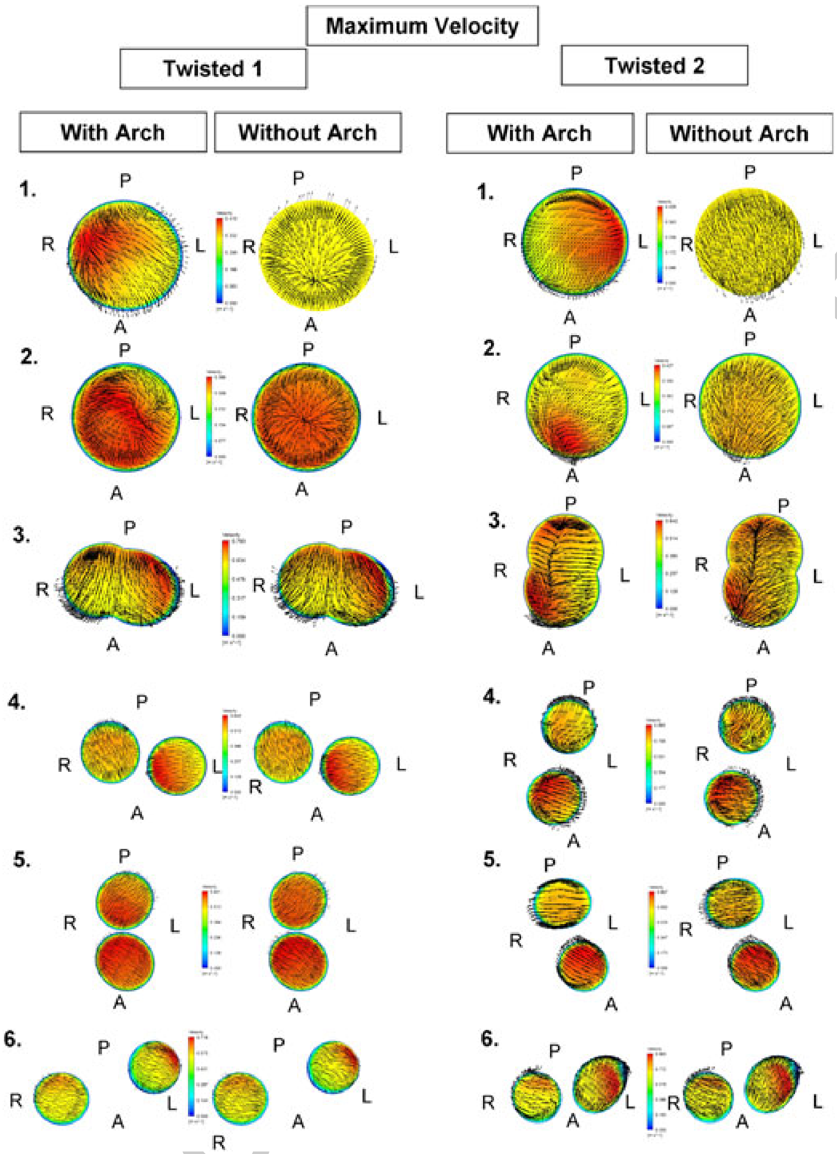

Figure 7. Velocity contour section plots along both twisted configurations with and without the full human aorta attached at maximum velocity.

(nontwisted 2), right/proximal (twisted 1) and left/proximal (twisted 2) when the stent graft models included the human aorta. Without the inclusion of the human aorta a flat velocity profile was imposed orthogonally to the stent graft inlet surfaces. Because of curvature and length of the proximal ends for all configurations the velocity profiles were very similar at the bifurcation point when comparing the models with the human aorta and those without. This similarity in velocity profiles can be seen along the distal legs. A similar finding was found during maximum deceleration with the velocity profiles being very similar at the bifurcation point.

There was less than 1% difference in drag force along one cardiac cycle when comparing the stent graft models with the inclusion of the human aorta to those without the human aorta.

The highest resultant drag force magnitude during the fifth cardiac cycle was recorded at $t = 0.4$ s, where blood pressure reached its peak value, and these were found to be 6.6 N for nontwisted 1, 8.8 N for nontwisted 2, 7.6 N for twisted 1 and 6.8 N for twisted 2. For all stent graft configurations the minimum drag force was in the X-direction and the maximum in the Z-direction. Both nontwisted leg configurations had the X component of drag force in the opposite direction when compared with

Copyright © 2012 John Wiley & Sons, Ltd.

DOI: 10.1002/cnm

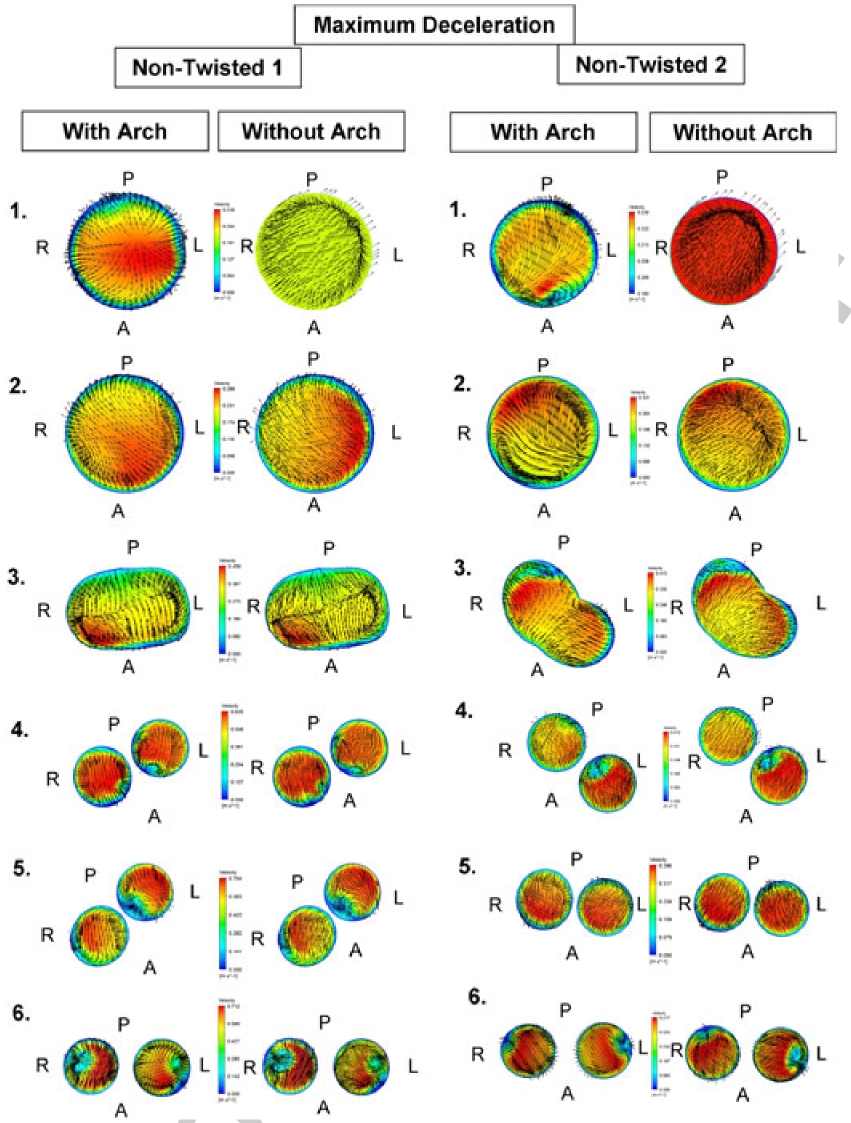

Color Online, B&W in Print

Figure 8. Velocity contour section plots along both nontwisted configurations with and without the full human aorta attached at maximum deceleration.

the twisted leg configurations. The spatial representation of the drag force vectors was computed for the maximum pressure as shown in Figure 10(F) and given in Table V. Figure 10(F) shows the orientation of the drag force resultant vector during one cardiac cycle. Figure 10(F) displays four closed loop drag force curves for all models with corresponding markers representing the start of the cycle, peak velocity and peak pressure. The drag force angle with respect to the X-axis varied between 65° and 105° at maximum blood pressure. The maximum variation in drag force angle for all configurations varied from 1.3° to 5°. From the spatial vector representation it was observed that the resultant drag force for all cases was changing its orientation during the cardiac cycle within one plane.

There was significant skewing and recirculation of the blood before the celiac arteries, which continued further downstream beyond the renal arteries under the influence of the aortic arch and the four branching arteries superior to each stent graft device. The complexity of the flow patterns, degree of skewness and secondary flows was influenced by the inclusion of the full human aorta with the seven branches proximal to the bifurcation but not within the distal legs. The realistic input boundary condition creates a moon-like skewing profile, which results in a greater recirculation

Copyright © 2012 John Wiley & Sons, Ltd.

DOI: 10.1002/cnm

Color Online, B&W in Print

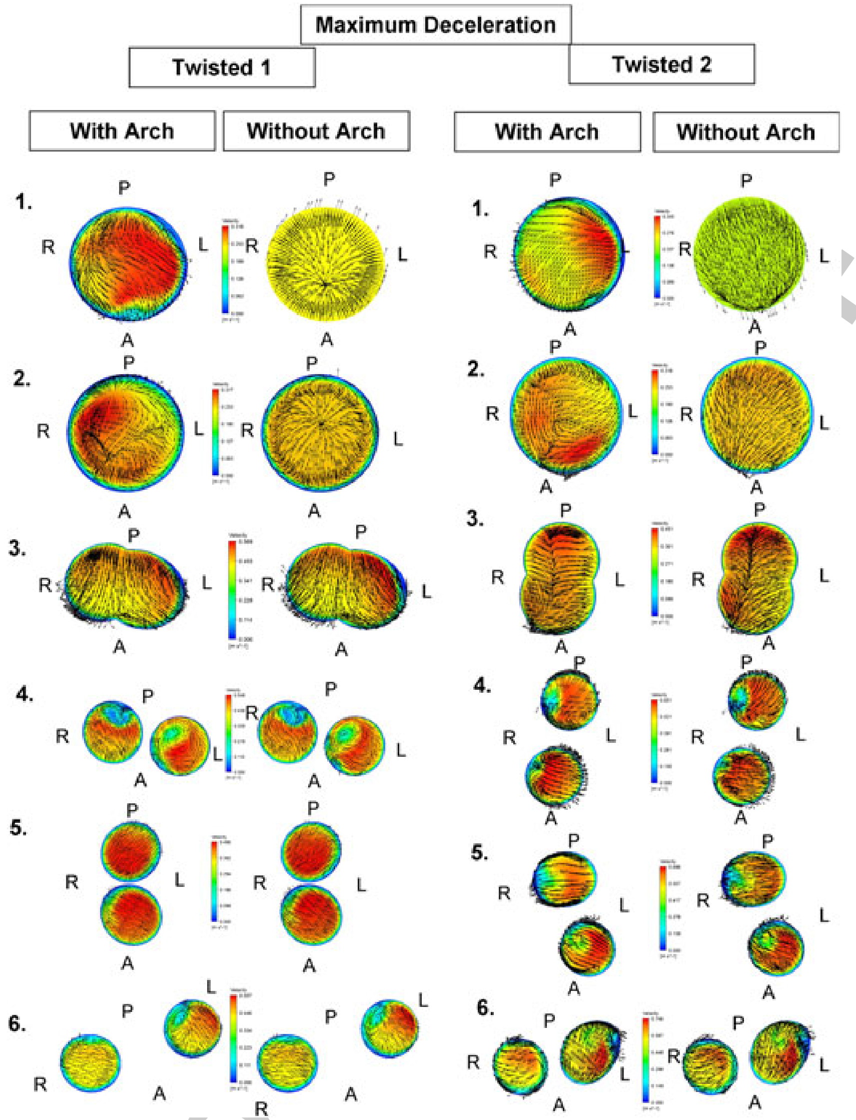

Figure 9. Velocity contour section plots along both nontwisted configurations with and without the full human aorta attached at maximum deceleration.

region in the left leg of the nontwisted 1 and twisted 2 configurations as shown in Figures 6 and 7. During the decelerating phase significant recirculations occurred along the main body of all stent graft models and in particular at the bifurcation point as shown in Figures 8 and 9, Sections 1 to 3. These recirculations are in agreement with the clinical findings of Wegener *et al*. [65] in which thrombus formation was reported within the main body of a bifurcated stent graft because of specific flow patterns that may be responsible for thrombus formation. They concluded that these flow disturbances were partly due to the large outflow of the renal arteries. This further emphasises the need to include the outflow vessels superior to the proximal end of the stent graft.

The main influencing factor for the velocity profiles through all the models are the geometrical differences that are associated with each model. It is known from the literature that curvature effects throughout the arterial system induces Dean forces that increase in magnitude with increasing Dean number [35, 41–43, 46]. Dean's number (*De*) can be used to assess the variation because of geometrical and hemodynamic effects along the axis of each model. Dean's number can be used to analyse the different geometrical differences associated with each model and hence predict which model will create the greatest skewness, recirculation and secondary velocities. Referring to

Copyright © 2012 John Wiley & Sons, Ltd.

DOI: 10.1002/cnm

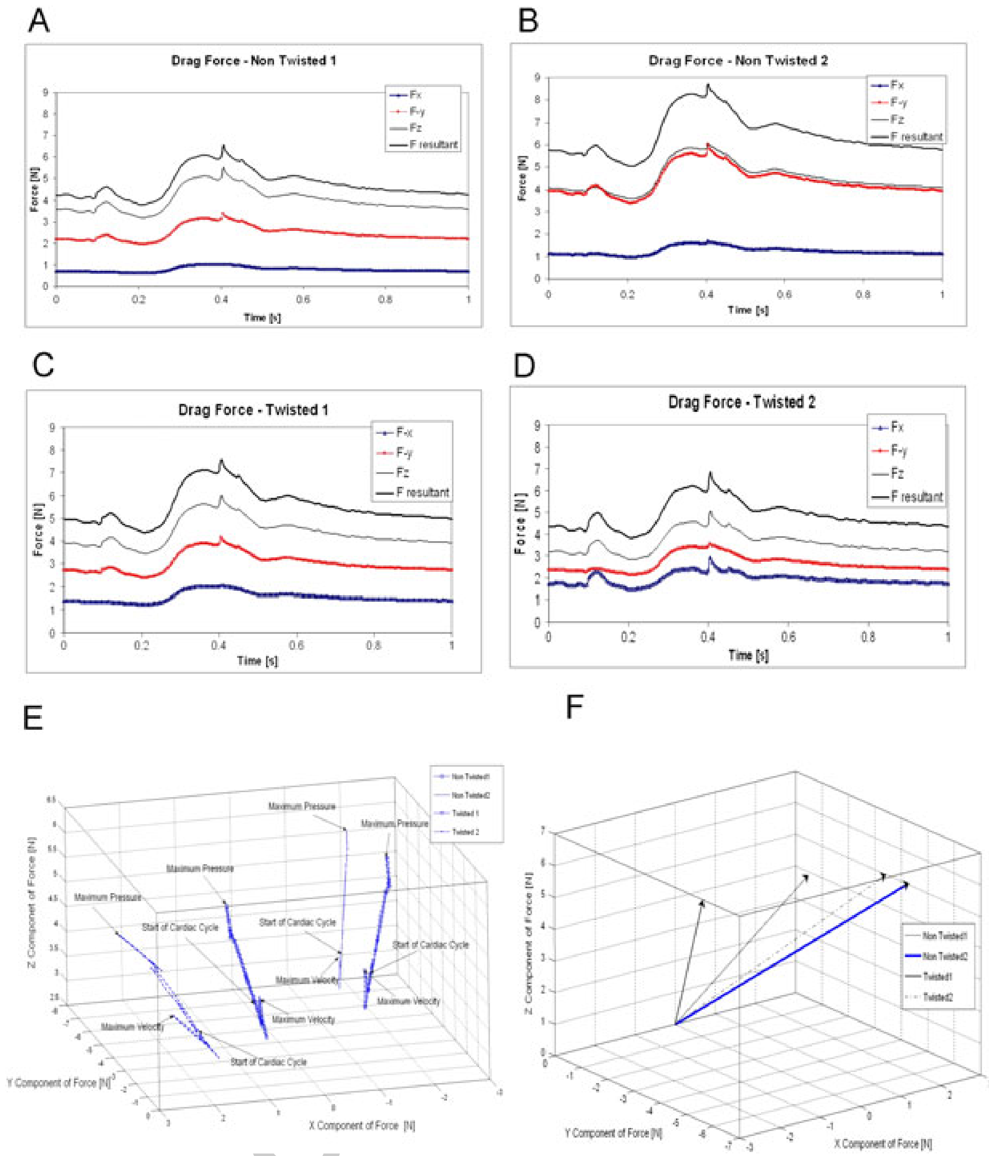

Figure 10. Drag force plots acting on the stent graft models: (A) nontwisted 1, (B) nontwisted 2, (C) twisted 1, (D) twisted 2, (E) 3D drag force orientation for all models over one cardiac cycle and (F) drag force resultant 3D vector plot for all models at maximum blood pressure.

Color Online, B&W in Print

Table V. Maximum drag force and orientation angles. φ is the maximum change in drag force angle over one cardiac cycle and θ is the maximum force orientation angle with respect to the X-axis.

Model	F_x [N]	F_y [N]	F_z [N]	F_r [N]	φ [°]	θ [°]
Nontwisted 1	1.0	–3.4	5.5	6.6	1.3	81.0
Nontwisted 2	1.7	–6.1	6.1	8.7	1.6	79.3
Twisted 1	–2.0	–4.1	~~6.00~~	7.6	1.6	105.7
Twisted 2	2.9	–3.5	5.1	6.8	5.0	64.7

Equation (1), Dean's number is inversely proportional to the radius of curvature and directly proportional to the radius of the lumen and Reynolds number. The out of plane curvature influences the local characteristics of the velocity profiles. The realistic geometries are characterised by varying radius of curvature and hence varying Dean's number. The radius of curvature and Dean's number can predict the location along the model in which the greatest secondary flows will occur.

Copyright © 2012 John Wiley & Sons, Ltd.

DOI: 10.1002/cnm

Therefore, these two parameters alone are needed when predicting device failure. As found by the Mann–Whitney nonparametric test nontwisted 1 had the highest Dean's number for the left leg while both nontwisted 1 and twisted 2 had the highest Dean's number for the right legs, which corresponded to greater secondary flows and recirculation regions especially during the maximum deceleration phase.

Stent graft failures are known to occur at bifurcation points. Stent graft thrombosis and micro-embolism are two complications associated with endovascular repair of AAAs [52]. Intraprosthetic thrombotic deposits within the iliac limbs were reported in 7% to 26% of cases [65–67] with stent graft limb occlusions occurring in 11% [68] and 16% [65] of reported cases. Several cases of fatal multi-organ failures have been linked to micro-embolism [66]. Failure at the bifurcation point and at the entrance to both iliac limbs could be caused by the increased secondary flows generated at the bifurcated junction, which results in the further skewing of the flow past the flow divider that creates a boundary layer. This skewing and flow separation in the iliac limbs may partly explain the recent reports of clinical failures in bifurcated stent graft devices because of thrombosis in the limb region [69]. The numerical results found here have shown that performance of stent grafts may be influenced by the local curvature along the iliac limbs. The radius of curvature along these limbs may aid in predicting where thrombotic deposits might occur because of increased secondary flows.

All endovascular devices used for AAA repair may migrate as a result of the pulsatile action of blood flow and pressure [70]. Some device manufacturers have defined migration as a proximal or distal stent graft movement more than 5 mm, or in other cases more than 10 mm [26]. From a mechanical point of view, the positional stability problem can be regarded as competition between the loads acting on the stent graft, called displacement forces or drag forces, and the radial forces that keep the device attached to the arterial wall. The drag force is determined by the geometry of the device, the hemodynamic state of the patient (i.e., hypertension, cardiac output, etc.) and the anatomy of the AAA. Risk of device failure may be reduced if the optimum configuration is found for any particular case. The curvature analysis of the diseased aorta can be an important tool in finding the best positioning of an endovascular device by identifying the areas of large Dean's number, which can then be taken into account when the AAA repair is performed. The resultant drag force magnitudes for both stent graft configurations were in agreement with the results of Molony *et al*. [71] who computationally studied 10 stent graft geometries and with the analytical results of Morris *et al*. [23]. Molony *et al*. [71] found the greatest drag force direction occurs at either the anterior (Y-component) or caudal (Z-component) similar to our nontwisted 2 configuration as shown in Figure 10(B).

The application of the structured hexahedral O-grid meshing technique with optimised mesh density, pulse cycle number, time step size and residues give the best possible solution for this numerical study. When compared with Womersley's solutions for straight tubes the O-grid structured grid can give an error of less than 2% when comparing the velocity profiles. For experimental flow studies through bifurcated geometries our group has shown good qualitative agreement with the velocity profiles with quantitative errors ranging from 2% to 15%.

This study did not take into account the effects of the stents that are normally positioned throughout the graft. Commercially available stent graft devices have either an exo-stent or endo-stent configuration. The exo-stent configuration has the stent on the outside of the graft and therefore does not interfere with the blood flow. It was found experimentally [52] that there was no significant difference between exo-stent and endo-stent configurations. Their studies showed that central flow in exo-stent configuration was smooth in the proximal end suggesting minimal effect of the stent on the overall hemodynamics. At the proximal end where the stent density was high, particles were trapped, which created a low velocity zone. A luminal layer usually covers the stent struts and this eliminates the effects the stent struts has on the flow [72]. Although the assumption of rigid walls was appropriate for modelling the arterial wall and rigid stent graft devices, the lumen of the aneurismal sac can be and most often is bordered by intra-luminal thrombus (ILT). ILT is known to be much more distensible than the aortic wall (either aneurysmal or nonaneurysmal). The movement of this ILT during a pulse cycle may influence the flow patterns both qualitatively and quantitatively. Future CFD analysis should incorporate a fluid structure interaction simulation to take into account the movement of the ILT/lumen boundary.

UNCORRECTED PROOF

Copyright © 2012 John Wiley & Sons, Ltd.
DOI: 10.1002/cnm

The clinician's decision for the positioning of a stent graft during endovascular repair may be a critical parameter, and should be taken into account when designing the optimum stent graft device. Both twisted stent graft models further promoted the spiral flow effect along its distal legs that was also present along the descending aorta. The stent graft models in this study had other model variations because of the variations in AAA morphology, which was different for each stent graft configuration. Future studies are required to fully assess the outcomes of nontwisted configurations versus twisted configurations. For the case of acute iliac angulations a crossed leg deployment may be the optimum positioning procedure for a bifurcated endovascular device to prevent iliac limb kinking.

Overall, the main influencing factors that affect stent graft computational blood flow modelling are the input boundary conditions and the out of plane curvature. The radius of curvature and Dean's number may be used to predict where the secondary flows would occur because of local changes in curvature.

In conclusion, the inclusion of the full human aorta with associated branches generates a highly skewed input flow field that continues downstream towards the bifurcation. Beyond the bifurcation the flow develops and has a very similar flow field to that without the inclusion of the full human aorta. There was less than a 1% variation in drag force when comparing the stent graft models with the human aorta to those without.

UNCORRECTED PROOF

ACKNOWLEDGEMENTS

The authors would like to acknowledge Mr Eamon G. Kavanagh, Consultant Vascular Surgeon, HSE Midwestern Regional Hospital, Limerick, Mr Prakash Madhavan, Consultant Vascular Surgeon, St. James Hospital, Dublin and the McGowan Institute for Regenerative Medicine, Pittsburgh, USA for providing the medical data used in this study. The would also like to acknowledge Strand 1, Department of Education in Ireland for funding this work.

REFERENCES

1. Brown PM, Zelt DT, Sobolev B. The risk of rupture in untreated aneurysms: the impact of size, gender, and expansion rate. *Journal of Vascular Surgery* 2003; **37**:280–284.
2. Vorp DA, Geest JPV. Biomechanical determinants of abdominal aortic aneurysm rupture. *Arteriosclerosis, Thrombosis, and Vascular Biology* 2005; **25**:1558–1566.
3. ~~Abdominal aortic aneurysms statistics. (Available from: http://www.pharmacistelink.com/lifeline/pdf/AbdominalAorticAneurysmStatistics.pdf) [Accessed on 14 March 2008].~~ ~~Q7~~
4. Alexander JJ. The pathobiology of aortic aneurysms. *Journal of Surgical Research* 2004; **117**:163–175.
5. Choke E, Cockerill G, Wilson WRW, Sayed S, Dawson J, Loftus I, Thompson MM. A review of biological factors implicated in abdominal aortic aneurysm rupture. *European Journal of Vascular and Endovascular Surgery* 2005; **30**:227–244.
6. Davies MJ. Aortic aneurysm formation: lessons from human studies and experimental models. *Circulation* 1998; **98**:193–195.
7. Fillinger M. Who should we operate on and how do we decide: predicting rupture and survival in patients with aortic aneurysm. *Seminars in Vascular Surgery* 2007; **20**:121–127.
8. Endovascular aneurysm repair and outcome in patients unfit for open repair of abdominal aortic aneurysm (EVAR trial 2): randomised controlled trial. *The Lancet* 2005; **365**:2187–2192. Q8
9. Greenhalgh RM, Kwong BL, Powell GP, Thompson JT. EVAR trial participants. comparison of endovascular aneurysm repair with open repair in patients with abdominal aortic aneurysm (EVAR trial 1), 30-day operative mortality results: randomised controlled trial. *Lancet* 2004; **364**:843–848.
10. Prinssen M, ~~Buth VE, Cuypers J, van Sambeek PW, Balm MR, *et al.*~~ A randomized trial comparing conventional and endovascular repair of abdominal aortic aneurysms. *The New England Journal of Medicine* 2004; **351**:1607–1618.
11. Endovascular aneurysm repair versus open repair in patients with abdominal aortic aneurysm (EVAR trial 1): randomised controlled trial. *The Lancet* 2005; **365**:2179–2186.
12. Brewster DC, Cronenwett JL, Hallett JW, Jr, Johnston KW, Krupski WC, Matsumura JS. Guidelines for the treatment of abdominal aortic aneurysms. Report of a subcommittee of the Joint Council of the American Association for Vascular Surgery and Society for Vascular Surgery. *Journal of Vascular Surgery* 2003; **37**:1106–1117.
13. Manning B, Hynes N, Kok N, Mahendran B, Sultan S. Abdominal aortic aneurysm repair in octogenarians versus younger patients in a tertiary referral center. *Journal of Vascular Surgery* 2005; **13**:275–285.
14. Marin ML, Hollier LH. *Endovascular Grafting: Advanced Treatment for Vascular Disease*. Futura Publishing Co., Inc: NY, 2000.
15. ~~Endovascular repair with a stent graft, 2009. (Available from: http://www.medtronic.eu) [Accessed on 5 March 2010].~~

Copyright © 2012 John Wiley & Sons, Ltd.
DOI: 10.1002/cnm

16. Ashton HA, Buxton MJ, Day NE, Kim LG, Marteau TM, Scott RA, Thompson SG, Walker NM. The Multicentre Aneurysm Screening Study (MASS) into the effect of abdominal aortic aneurysm screening on mortality in men: a randomised controlled trial. *Lancet* 2002; **360**:1531–1539.
17. ~~Surgical & Radiology Associates, Endovascular Aneurysm Repair, 2010. (Available from: http://crlsurgical.com/surgical/aneurysmRepair.php) [Accessed on 15 June 2010].~~
18. Darling RC, Messina CR, Brewster DC, Ottinger LW. Autopsy study of unoperated abdominal aortic aneurysms. The case for early resection. *Circulation* 1977; **56**:II161–II164.
19. Faxon DP, Fuster V, Libby P, Beckman JA, Hiatt WR, Thompson RW, Topper JN, Annex BH, Rundback JH, Fabunmi RP, Robertson RM, Loscalzo J. Atherosclerotic vascular disease conference: writing group III: pathophysiology. *Circulation* 2004; **109**:2617–2625.
20. Hinnen JW, Koning OH, van Bockel JH, Hamming JF. Aneurysm sac pressure after EVAR: the role of endoleak. *European Journal of Vascular and Endovascular Surgery* 2007; **34**:432–443.
21. Li Z, Kleinstreuer C. Computational analysis of type II endoleaks in a stented abdominal aortic aneurysm. *Journal of Biomechanics* 2006; **39**:2573–2582.
22. Li Z, Kleinstreuer C. Effects of major endoleaks on a stented abdominal aortic aneurysm model. *Journal of Biomechanical Engineering* 2006; **128**:59–68.
23. Morris LG, Delassus P, Walsh M, McGloughlin TM. A mathematical model to predict the in vivo pulsatile drag forces acting on bifurcated stent grafts in endovascular treatment of abdominal aortic aneurysms (AAA). *Journal of Biomechanics* 2004; **37**:1087–1095.
24. Molony DS, Callanan A, Morris LG, Doyle BJ, Walsh MT, McGloughlin TM. Geometrical enhancements for abdominal aortic stent-grafts. *Journal of Endovascular Therapy* 2008; **15**:518–529.
25. Q9 Bosman WMPF, TJvd S, SuÃ¡rez DR, Hinnen JW, Valstar ER, Hamming JF. The proximal fixation strength of modern EVAR grafts in a short aneurysm neck. An in vitro study. *European Journal of Vascular and Endovascular Surgery* 2010; **39**:187–192.
26. Figueroa CA, Taylor CA, Yeh V, Chiou AJ, Gorrepati ML, Zarins CK. Preliminary 3D computational analysis of the relationship between aortic displacement force and direction of endograft movement. *Journal of Vascular Surgery* 2010; **51**:1488–1497.
27. Figueroa CA, Yeh TC, Chiou AJ, Zarins CK. Effect of curvature on displacement forces acting on aortic endografts: a 3-dimensional computational analysis. *Journal of Endovascular Therapy* 2009; **16**:284–294.
28. Q10 ~~Li,~~ Kleinstreuer C. Fluid-structure interaction effects on sac-blood pressure and wall stress in a stented aneurysm. *Journal of Biomechanical Engineering* 2005; **127**:662–671.
29. Morris L, Delassus P, Grace P, Wallis F, Walsh M, McGloughlin T. Effects of flat, parabolic and realistic steady flow inlet profiles on idealised and realistic stent graft fits through abdominal aortic aneurysms (AAA). *Medical Engineering & Physics* 2006; **28**:19–26.
30. Resch T, Malina M, Linbald B, Malina J, Brunkwall J, Ivancev K. The impact of stent design on proximal stent-graft fixation in the abdominal aorta: an experimental study. *European Journal of Vascular and Endovascular Surgery* 2000; **20**:190–195.
31. ~~Bosman WMPF, TJvd S, SuÃ¡rez DR, Hinnen JW, Valstar ER, Hamming JF. The proximal fixation strength of modern EVAR grafts in a short aneurysm neck. An in vitro study. *European Journal of Vascular and Endovascular Surgery* 2010; **39**:187–192.~~
32. Corbett TJ, Molony DS, Callanan A, McGloughlin TM. The effect of vessel material properties and pulsatile wall motion on the fixation of a proximal stent of an endovascular graft. *Medical Engineering & Physics* 2010; **33**:106–111.
33. Shahcheraghi N, Dwyer HA, Cheer AY, Barakat AI, Rutaganira T. Unsteady and three-dimensional simulation of blood flow in the human aortic arch. *Journal of Biomechanical Engineering* 2002; **124**:378–87.
34. Tortoli P, Bambi G, Guidi F, Muchada R. Toward a better quantitative measurement of aortic flow. *Ultrasound in Medicine & Biology* 2002; **28**:249–257.
35. Chandran KB. Flow dynamics in the human aorta. *Journal of Biomechanical Engineering* 1993; **115**:611–616.
36. Yearwood TL. Physiological pulsatile flow experiments in a model of the human aortic arch. *Journal of Biomechanics* 1984; **15**(9):683–704.
37. Talbot L. Pulsatile entrance flow in a curved pipe. *Journal of Fluid Mechanics* 1983; **127**:1–25.
38. Chandran KB. Experimental study of physiologcial pulsatile flow in a curved tube. *Journal of Fluid Mechanics* 1981; **111**:59–85.
39. Q11 Pedley TJ. *The fluid mechanics of large blood vessels*. Cambridge University Press, 1980.
40. Q12 Morris L, Delassus P, Callanan A, Walsh M, Wallis F, Grace P, McGloughlin T. 3-D numerical simulation of blood flow through models of the human aorta. *Journal of Biomechanical Engineering* 2005; **127**:767–775.
41. Q13 Papaharilaou Y. The influence of [illegible]-plane geometry on pulsatile flow within a distal end-to-side anastomosis. *Journal of Biomechanics* 2002; **35**.
42. Q14 Myers K, Devine T, Barras C, Self G. Endoluminal Versus Open Repair for Abdominal Aortic Aneurysms, 2001. (Available from: http://www.fac.org.ar/scvc/llave/interven/myers/myersi.htm).
43. Naruse T, Tanishita K. Large curvature effect on pulsatile entrance flow in a curved tube: Model experiment simulating blood flow in an aortic arch. *Journal of Biomechanical Engineering* 1996; **118**:180–186.
44. Moore JE Jr, Ku DN. Pulsatile velocity measurements in a model of the human abdominal aorta under resting conditions. *Journal of Biomechanical Engineering* **116**:337–346.

UNCORRECTED PROOF

Copyright © 2012 John Wiley & Sons, Ltd.
DOI: 10.1002/cnm

45. Moore JE Jr, Ku DN. Pulsatile velocity measurements in a model of the human abdominal aorta under simulated exercise and postprandial conditions. *Journal of Biomechanical Engineering* 1994; **116**:107–111.
46. Pedersen EM, Sung HW, Yoganathan AP. Influence of abdominal aortic curvature and resting versus exercise conditions on velocity fields in the normal abdominal aortic bifurcation. *Journal of Biomechanical Engineering* 1994; **166**:347–353.
47. Moore JE Jr, Ku DN, Zarins CK, Glagov S. Pulsatile flow visualization in the abdominal aorta under differing physiologic conditions: implications for increased susceptibility to atherosclerosis. *Journal of Biomechanical Engineering* 1992; **114**:391–397.
48. Lin YH. Ultrasonic backscattering from porcine whole blood of varying hematocrit and shearrate under pulsatile flow. *Ultrasound in Medicine & Biology* 1999; **25**(7):1151–1158.
49. Lee D, Chen JY. Numerical simulation of steady flow fields in a model of abdominal aorta with its peripheral branches. *Journal of Biomechanics* 2002; **35**:1115–1122.
50. Taylor CA, Hughes TJR, Zarins CK. Effect of exercise on hemodynamic conditions in the abdominal aorta. *Journal of Vascular Surgery* 1999; **26**(6):1070–1089.
51. Taylor CA, Hughes TJR, Zarins CK. Effect of exercise on hemodynamic conditions in the abdominal aorta. *Journal of Vascular Surgery* 1998; **29**:1077–1089.
52. Chong CK, How TV. Flow patterns in an endovascular stent-graft for abdominal aortic aneurysm repair. *Journal of Biomechanics* 2004; **37**:89–97.
53. Walsh PW, Chin-Quee S, Moore JE Jr. Flow changes in the aorta associated with the deployment of a AAA stent graft. *Medical Engineering & Physics* 2003; **25**:299–307.
54. Shipkowitz T, Rodgers VGJ, Frazin JF, Chandran KB. Numerical study on the effects of secondary flow in the human aorta on local shear stresses in abdominal branches. *Journal of Biomechanics* 2000; **33**:717–728.
55. Bogren HG, Buonocore MH. Helical-shaped streamlines do not represent helical flow. *Radiology* 2010; **257**:895–896.
56. Cheng CP, Herfkens RJ, Taylor CA. Comparison of abdominal aortic hemodynamics between men and women at rest and during lower limb exercise. *Journal of Vascular Surgery* 2003; **37**:118–123.
57. Tortoli P, Bambi G, Guidi F, Muchada R. Toward a better quantitative measurement of aortic flow. *Ultrasound in Medicine & Biology* 2002; **28**(2):249–257.
58. Molony D, Callanan A, Kavanagh E, Walsh M, McGloughlin T. Fluid-structure interaction of a patient-specific abdominal aortic aneurysm treated with an endovascular stent-graft. *BioMedical Engineering OnLine* 2009; **8**:24.
59. Cheng CP, Parker D, Taylor CA. Quantification of wall shear stress in large blood vessels using Lagrangian interpolation functions with cine phase-contrast magnetic resonance imaging. *Annals of Biomedical Engineering* 2002; **30**:1020–1032.
60. Moore JE Jr, Ku DN. Pulsatile velocity measurements in a model of the human abdominal aorta under resting conditions. *Journal of Biomechanical Engineering* 1994; **116**:337–346.
61. Biasetti J. Blood flow and coherent vortices in the normal ane[...]atic aortas: A fluid dynamical approach to intra-luminal thrombus formation. *Journal of Royal Society* 2011. Q15
62. Nerem RM, Rumberger M, Gross DR, Hamlin RL, Geiger GL. Hot-film anemometry velocity measurements of arterial blood flow in horses. *Circulation Research* 1974; **10**:301–313.
63. Falsetti H, Kiser KM, Francis GP, Belmore ER. Sequential velocity development in the ascending and descending aorta of the dog. *Circulation Research* 1972; **21**:328–338.
64. Seed WA. Velocity patterns in the aorta. *Cardiovascular Research* 1971; **5**:319–330.
65. Wegener M, ~~GÃrich J, KrÃmer S,~~ Fleiter T, Tomczak R, Scharrer-Pamler R, Kapfer X, Brambs HJ. Thrombus formation in aortic endografts. *Journal of Endovascular Therapy* 2001; **8**:372–379. Q16
66. Parodi JC. Endovascular repair of abdominal aortic aneurysms and other arterial lesions. *Journal of Vascular Surgery* 1995; **21**:549–557.
67. Chong CK, How TV, Harris PL. Flow visualization in a model of a Bifurcated Stent-Graft. *Journal of Endovascular Therapy* 2005; **12**:435–445.
68. Jacobowitz GR, Lee AM, Riles TS. Immediate and late explantation of endovascular aortic grafts: The Endovascular technologies experience. *Journal of Vascular Surgery* 1999; **29**:309–316.
69. Becquemin JP, Lapie V, Favre JP, Rousseau H. Mid-term results of a second generation bifurcated endovascular graft for abdominal aortic aneurysm repair: The French vanguard trial. *Journal of Vascular Surgery* 1999; **30**:209–218.
70. Nabi D, Murphy EH, Pak J, Zarins CK. Open surgical repair after failed endovascular aneurysm repair: Is endograft removal necessary? *Journal of Vascular Surgery* 2009; **50**:714–721.
71. Molony DS, Kavanagh EG, Madhaven P, Walsh MT, McGloughlin T. A Computational study of the magnitude and direction of migration forces in patient-specific abdominal aortic aneurysm stent-grafts. *European Journal of Vascular and Endovascular Surgery* 2010; **40**:332–339.
72. Malina M, Brunkwall J, Ivancev K, Jonsson J, Malina J, Lindblad B. Endovascular healing is inadequate for fixation of dacron stent-grafts in human aortoiliac vessels. *European Journal of Vascular and Endovascular Surgery* 2000; **19**(1):5–11.
73. ~~Shahcheraghi N, Dwyer HA, Cheer AY, Barakat AI, Rutaganira T. Unsteady and three-dimensional simulation of blood flow in the human aortic arch. *Journal of Biomechanical Engineering* 2002; **12**:378–387.~~ ~~Q17~~

UNCORRECTED PROOF

Copyright © 2012 John Wiley & Sons, Ltd.

DOI: 10.1002/cnm

Research Article

Hemodynamic variations due to spiral blood flow through four patient-specific bifurcated stent graft configurations for the treatment of abdominal aortic aneurysms

Florian Stefanov, Tim McGloughlin, Patrick Delassus, and Liam Morris

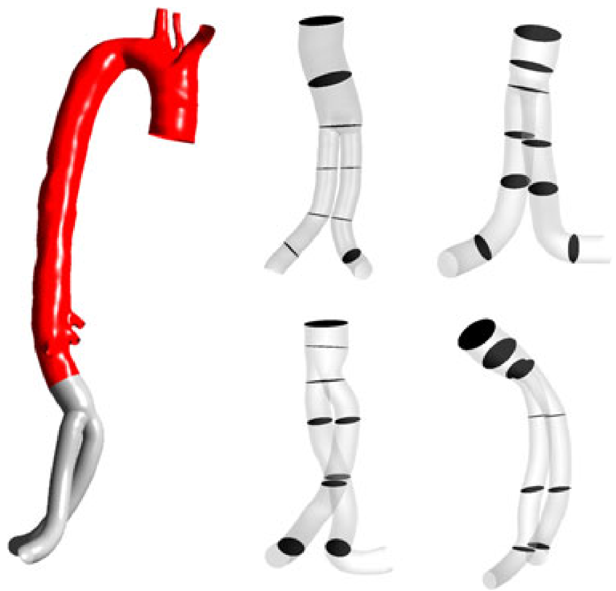

Q18 ■■

Author Query Form

Journal: International Journal for Numerical Methods in Biomedical Engineering

Article: cnm_2525

Dear Author,

During the copyediting of your paper, the following queries arose. Please respond to these by annotating your proofs with the necessary changes/additions.

- If you intend to annotate your proof electronically, please refer to the E-annotation guidelines.
- If you intend to annotate your proof by means of hard-copy mark-up, please refer to the proof mark-up symbols guidelines. If manually writing corrections on your proof and returning it by fax, do not write too close to the edge of the paper. Please remember that illegible mark-ups may delay publication.

Whether you opt for hard-copy or electronic annotation of your proofs, we recommend that you provide additional clarification of answers to queries by entering your answers on the query sheet, in addition to the text mark-up.

Query No.	Query	Remark
Q1	AUTHOR: three-dimensional. Is this the correct definition of 3D? Please change if incorrect.	
Q2	AUTHOR: Please provide manufacturer name, city, state (if US), and country for Dell Precision T3500.	
Q3	AUTHOR: As per journal style, Reference citations was in numbered format. Dean, 1927;1928 was not included in Reference list. Please check.	
Q4	AUTHOR: Please provide developer name, city, state, (if US), and country for MIMICS.	
Q5	AUTHOR: Please provide developer name, city, state, (if US), and country for MATLAB V7.0.1.	
Q6	AUTHOR: ‘geometers’ changed to ‘geometries’. Please check if this is correct.	
Q7	AUTHOR: Please check presentation if correct for References 3, 15 and 17.	
Q8	AUTHOR: Please provide list of all authors for References 8, 10 and 11.	
Q9	AUTHOR: Reference 25 was duplicated in Reference 31. Please check.	
Q10	AUTHOR: Please check capturing of author names if correct for Reference 28.	
Q11	AUTHOR: Please provide city location of the publisher for Reference 39.	

Q12	AUTHOR: Please check if page range for references 40, 44, 45, 47, 56 and 59 are presented correctly.	
Q13	AUTHOR: Please provide page range and issue number for reference 41.	
Q14	AUTHOR: Please provide "access on" date for reference 42.	
Q15	AUTHOR: If reference 61 is now published online please provide DOI infomation. If published in print please provide volume number, issue number and page range.	
Q16	AUTHOR: Please check if author names are presented properly in reference 65.	
Q17	AUTHOR: Reference 73 was not cited in the text. Please indicate where it should be cited or delete it from the reference list.	
Q18	AUTHOR: Please provide a short 'GTOC' abstract (maximum 80 words or 3 sentences) summarizing the key findings presented in the paper for Table of Content (TOC) entry.	

WILEY-BLACKWELL

USING e-ANNOTATION TOOLS FOR ELECTRONIC PROOF CORRECTION

Required software to e-Annotate PDFs: Adobe Acrobat Professional or Adobe Reader (version 7.0 or above). (Note that this document uses screenshots from Adobe Reader X)
The latest version of Acrobat Reader can be downloaded for free at: http://get.adobe.com/uk/reader/

Once you have Acrobat Reader open on your computer, click on the Comment tab at the right of the toolbar:

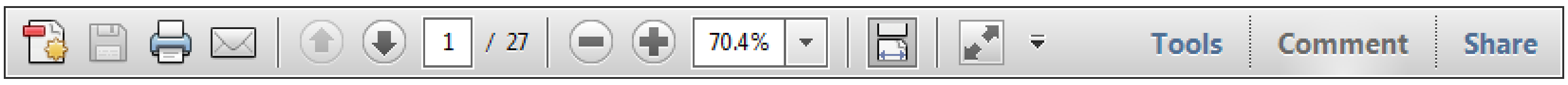

This will open up a panel down the right side of the document. The majority of tools you will use for annotating your proof will be in the Annotations section, pictured opposite. We've picked out some of these tools below:

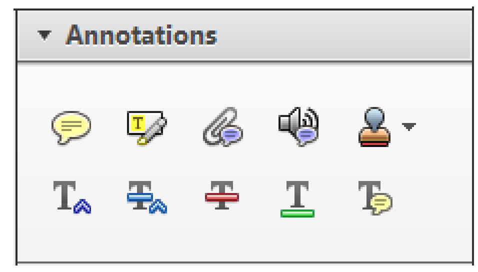

1. Replace (Ins) Tool – for replacing text.

Strikes a line through text and opens up a text box where replacement text can be entered.

How to use it

- Highlight a word or sentence.
- Click on the Replace (Ins) icon in the Annotations section.
- Type the replacement text into the blue box that appears.

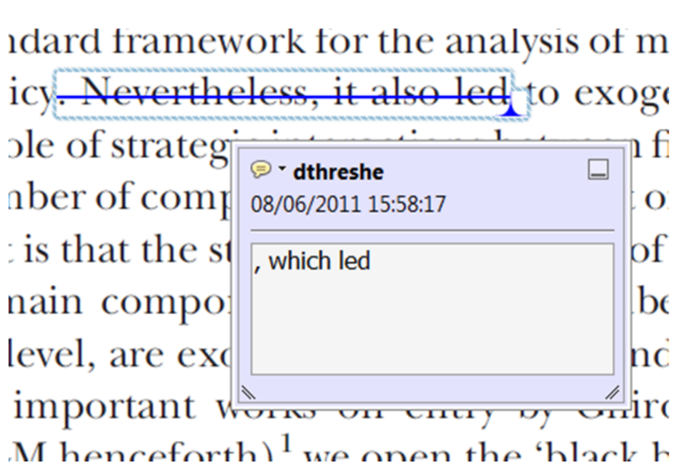

2. Strikethrough (Del) Tool – for deleting text.

Strikes a red line through text that is to be deleted.

How to use it

- Highlight a word or sentence.
- Click on the Strikethrough (Del) icon in the Annotations section.

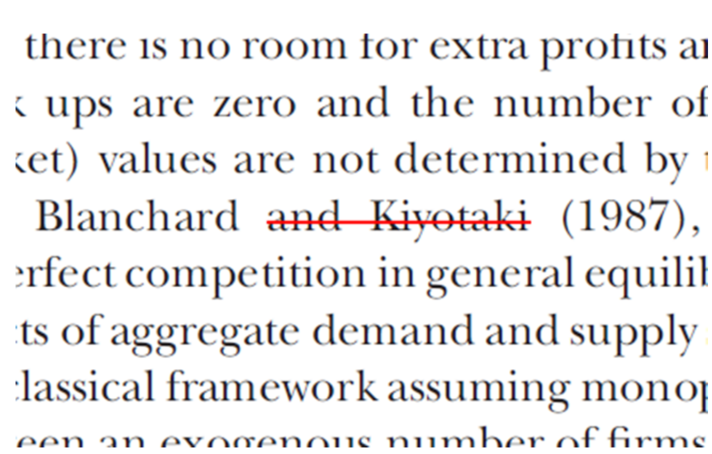

3. Add note to text Tool – for highlighting a section to be changed to bold or italic.

Highlights text in yellow and opens up a text box where comments can be entered.

How to use it

- Highlight the relevant section of text.
- Click on the Add note to text icon in the Annotations section.
- Type instruction on what should be changed regarding the text into the yellow box that appears.

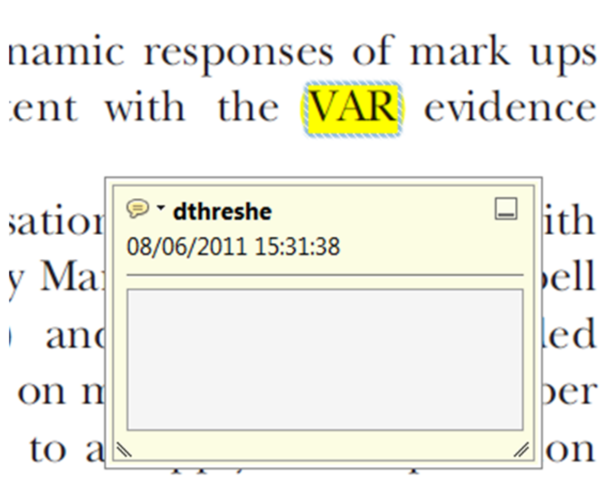

4. Add sticky note Tool – for making notes at specific points in the text.

Marks a point in the proof where a comment needs to be highlighted.

How to use it

- Click on the Add sticky note icon in the Annotations section.
- Click at the point in the proof where the comment should be inserted.
- Type the comment into the yellow box that appears.

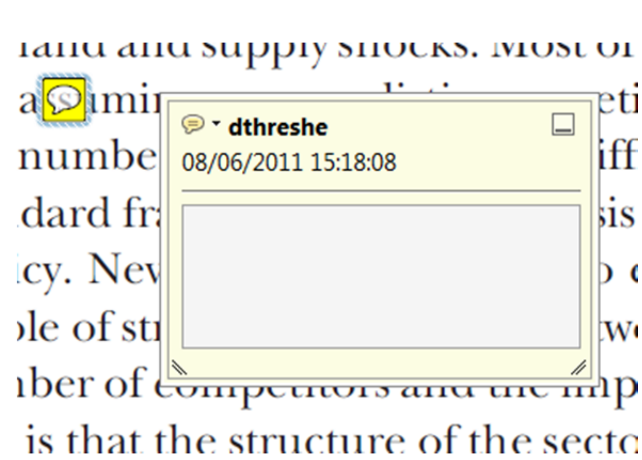

USING e-ANNOTATION TOOLS FOR ELECTRONIC PROOF CORRECTION

5. Attach File Tool – for inserting large amounts of text or replacement figures.

Inserts an icon linking to the attached file in the appropriate pace in the text.

How to use it

- Click on the Attach File icon in the Annotations section.
- Click on the proof to where you'd like the attached file to be linked.
- Select the file to be attached from your computer or network.
- Select the colour and type of icon that will appear in the proof. Click OK.

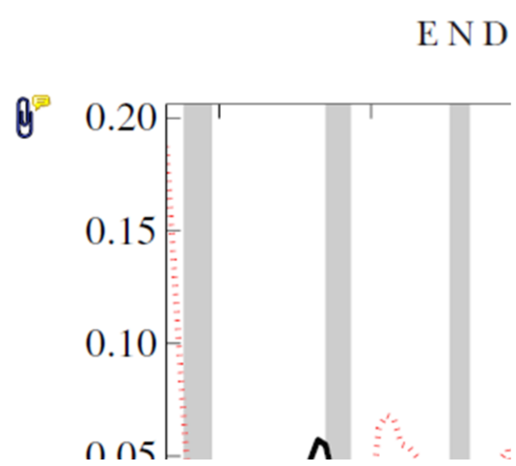

6. Add stamp Tool – for approving a proof if no corrections are required.

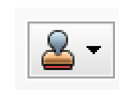

Inserts a selected stamp onto an appropriate place in the proof.

How to use it

- Click on the Add stamp icon in the Annotations section.
- Select the stamp you want to use. (The Approved stamp is usually available directly in the menu that appears).
- Click on the proof where you'd like the stamp to appear. (Where a proof is to be approved as it is, this would normally be on the first page).

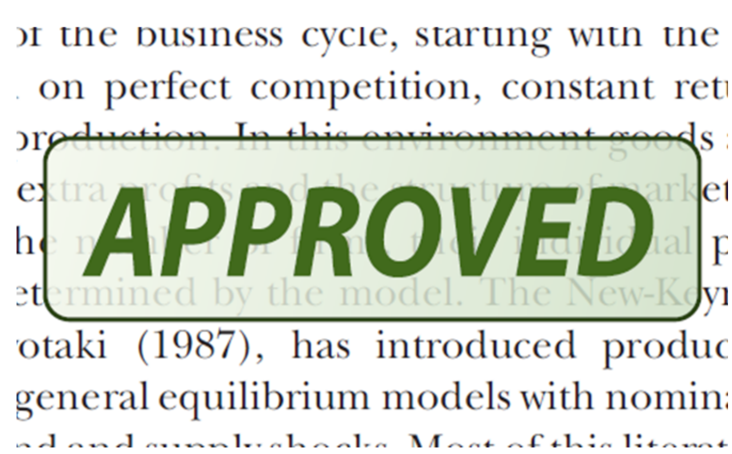

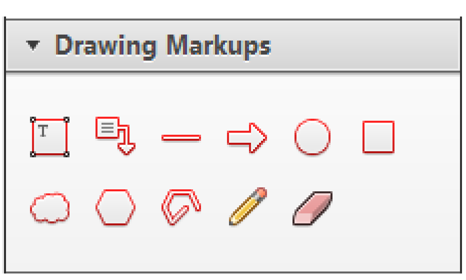

7. Drawing Markups Tools – for drawing shapes, lines and freeform annotations on proofs and commenting on these marks.

Allows shapes, lines and freeform annotations to be drawn on proofs and for comment to be made on these marks..

How to use it

- Click on one of the shapes in the Drawing Markups section.
- Click on the proof at the relevant point and draw the selected shape with the cursor.
- To add a comment to the drawn shape, move the cursor over the shape until an arrowhead appears.
- Double click on the shape and type any text in the red box that appears.

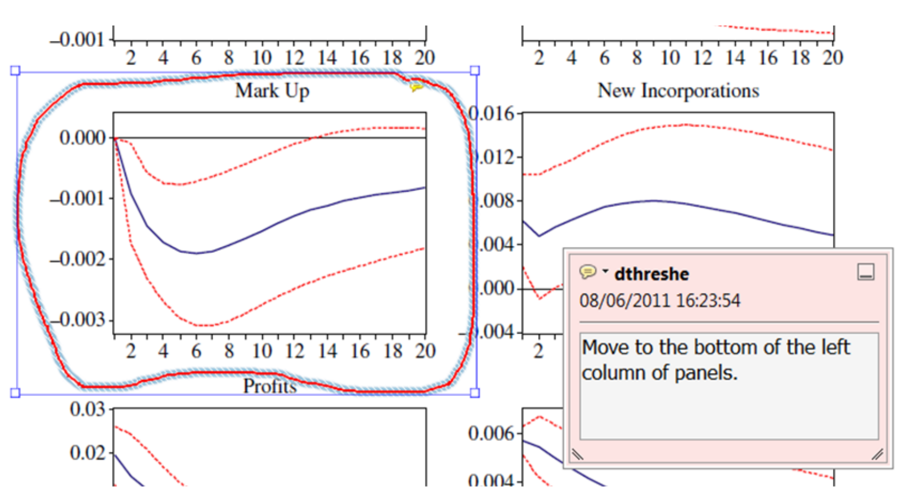

For further information on how to annotate proofs, click on the Help menu to reveal a list of further options: